



Investigations on Deposition Geometry and Mechanical Properties of Wire Arc Additive Manufactured Inconel 625

Ashish Kumar² · Kuntal Maji¹ · Ankit Shrivastava³

Received: 10 May 2022 / Revised: 20 December 2022 / Accepted: 18 April 2023 / Published online: 29 May 2023
© The Author(s), under exclusive licence to Korean Society for Precision Engineering 2023

Abstract

In this article, deposition geometry and mechanical properties of Inconel 625 alloy fabricated by wire arc additive manufacturing (WAAM) using gas metal arc welding principle were investigated. Parametric study and optimization of deposition geometry expressed in terms of width, height and cross-sectional area, were carried out considering the input variables such as voltage, wire feed rate, travel speed, and gas flow rate based on Box–Behnken design of experiments and response surface methodology. Mechanical properties of WAAM Inconel 625 were investigated using tensile testing, microhardness tests and fracture morphology of deposited thin wall geometry of Inconel 625. Tensile tests of samples were prepared in different orientations showed anisotropy existed in mechanical properties of the deposited wall, and the tensile properties of longitudinal direction were seen to be higher than the other two directions. Also, the tensile strength of longitudinal direction was highest near-substrate region and successively decreased towards the built direction. Microhardness study in different locations of the deposited wall showed highest value at the bottom region and successively reduced values along the built direction. Fracture morphology and microstructures with compositional analysis were performed on the fabricated wall structure using SEM. The microstructures of Inconel 625 were composed of columnar dendritic structure and tensile specimen fractures showed sharp tearing edges and dimpled surfaces indicative of good layer bonding with ductile failure morphology.

Keywords Wire arc additive manufacturing · Super alloy · Deposition geometry · Mechanical properties · Anisotropy · Heterogeneity

1 Introduction

Wire arc additive manufacturing (WAAM) technique comes under the category of directed energy deposition (DED). Wire plus arc based additive manufacturing technique

provide high deposition rate, suitable for large and complex geometry, required low material cost with economical manufacturing equipment costs and waste of material in the form of scrap is incredibly low. That way WAAM technique is more convenient and useful with other AM technique for metal-based deposition. The most generally utilized welding process incorporated with the WAAM technology are gas metal arc welding (GMAW), gas tungsten arc welding (GTAW), and plasma arc welding (PAW). GMAW is the most widely recognized choice of electrical thermal heat source because of its immediate feeding of wire spool into the deposition zone, the wire is coaxial with the welding torch.

Inconel 625 is a super alloy comes under the family of austenitic nickel–chromium-based alloy. The alloy has excellent corrosion resistance, oxidation resistance, and proper combination of mechanical properties: yield strength, tensile strength, hardness. The product made by Inconel materials was more expensive to fabricate using traditional method. In traditional manufacturing method lot of materials was wasted in the form of scrap. Therefore,

✉ Kuntal Maji
kuntalmaji.prod@nitjsr.ac.in

Ashish Kumar
akumar_mech@jspmrscoe.edu.in

Ankit Shrivastava
ankit.shrivastava@outlook.in

¹ Production and Industrial Engineering Department, National Institute of Technology Jamshedpur, Jharkhand 831 014, India

² Mechanical Engineering Department, JSPM's Rajarshi Shahu College of Engineering Pune, Maharashtra 411033, India

³ Materials Processing and Microsystems Laboratory, CSIR-Central Mechanical Engineering Research Institute, Durgapur 713209, India

WAAM was a comprisable manufacturing process to fabricate components near net shape.

Various types of function were used by some researcher to model the bead geometry in WAAM process under different processing conditions for various materials. For example, Gaussian, logistic, parabola, sine function used by Cao et al. [1] and sine function was found to best fit the bead profile. Circular arc, parabola, and cosine function to predict weld bead shape used by Xiong et al. [2]. Ding et al. [3] found that parabola and cosine models could represent single weld bead geometry with resembling accuracy. Kumar et al. [4] utilized neural network back-propagation technique for the modelling of bead geometry using CMT welding of aluminium alloy 4043 (5% silicon). The input process parameters are voltage, current, travel speed and shielding gas flow rate to predict three output parameters, penetration, bead width, and height. Youheng et al. [5] tried to optimize the WAAM process parameters. The multi-objective optimization was conducted by using response surface optimization to minimize the heat input, maximize the ratio of width to reinforcement, and minimize the current and voltage. The results show that the optimized sample surface appearance was smooth and no visible defects. Sarathchandra et al. [6] investigated the parameters effect on SS304 weld bead geometry deposited using cold metal transfer (CMT) WAAM. A second order regression model was developed for bead width, bead height, penetration, and dilution in terms of the considered input parameters, i.e., current, standoff distance, and weld speed. Dinovitzer et al. [7] concluded that travel speed and current was the most significant influence on the bead geometry for deposition of Hastelloy X using TIG based WAAM. Bharat et al. [8] optimized the process parameter for deposition of Inconel 825 using Taguchi method through WAAM. A linear regression model was established for bead width to construct thick and thin walls with minimizing porosity, cracks, and discontinuity of weld bead. Kumar et al. [9] tried to optimize the deposition process to obtain a smooth layer in GMAW based WAAM. The travel speed was seen to influence the shape of the deposited layer, and the shielding gas flow rate had the least effect on the layer geometry. Le et al. [10] optimized the process parameters using response surface methodology (RSM) for deposition of 308L steel through WAAM. The single bead deposited at optimal parameters was produced smooth and uniform bead at lower heat input. Tonelli et al. [11] deposited the plates of aluminum having grade ER 5183 using WAAM process and investigated the mechanical properties in three different directions. They found that the mechanical properties are higher in longitudinal direction in compared to other two direction and diagonal direction has lowest mechanical properties. Abdelall et al. [12] applied the new layer

deposition technique to deposit E6013 low carbon steel at different inclination angles. They found that the anisotropic behaviour reduces when deposition angles of 30° and 45° are used.

The mechanical and metallurgical characterizations of Austenitic Nickel–Chromium-Based alloys fabricated by WAAM were also studied by some researchers. Dinda et al. [13] studied the microstructure and thermal stability of Inconel 625 superalloy fabricated through laser aided direct metal deposition. They found that the resulting microstructure was columnar dendritic, that grew epitaxially from the substrate in direction of laser scan. Xu et al. [14] investigated the microstructure and mechanical properties of Inconel 625 alloy deposited through pulsed plasma arc deposition (PPAD). It was found that sample deposited through inter-pass cooling strategy (ICS) has improved surface quality, mechanical property and microstructure compared to the case of continuous deposition strategy (CDS). The microstructures and mechanical properties of Inconel 625 alloy manufactured by PPAD-WAAM were also investigated by Xu et al. [15]. It was concluded that microstructures exhibited homogenous columnar dendrite structure, which grow epitaxially along the deposition direction. The phase analysis revealed the precipitations of Laves phase, MC carbides (NbC, TiC) and needle like- δ -Ni₃Nb. The microhardness at the interface region was slightly higher than that at other regions due to highly refined structure at the interface region. Li et al. [16] investigated the microstructure of Inconel 625 alloy samples fabricated through selective laser melting (SLM) process and the mechanical properties were studied under different heat treatment conditions. It was concluded that the microstructure of molten pool was composed of elongated columnar crystal and primary dendrite arm space was two times smaller as compared with the traditional casting process due to rapid solidification. Wang et al. [17] manufactured Inconel 625 components through GTAW based WAAM process and investigated the microstructure and mechanical properties based on the location effect. The authors concluded that microstructure near substrate region is columnar dendrite followed epitaxially along the built direction. They also found undesirable laves phase higher near the top region due to that the mechanical properties near the top region were lower in comparison to substrate region. Hack et al. [18] investigated the mechanical, metallurgical and corrosion properties of Inconel 625 alloy parts manufactured using the laser powder bed fusion (L-PBF) manufacturing process. It was concluded that the manufactured parts exhibited better strength, fracture toughness and impact toughness compared with parts manufactured through conventional forging processes. Tanvir et al. [19, 20] found that the microstructure of Inconel 625 alloy exhibited columnar

dendrite structure and the undesirable laves phase found in as deposited condition that decrease the strength and increases the brittleness. They also concluded that the mechanical properties of WAAM manufactured Inconel 625 component was improved by 2 h annealing procedure. The annealing heat treatment was enhanced the ultimate tensile strength but no changes in yield strength was found. Yangfan et al. [21] investigated the influence of torch travel speed on microstructure and mechanical properties of the CMT-WAAM of Inconel 625 alloy. They found that the tensile properties and micro-hardness increases with increases of travel speed. The microstructures varying along the build direction from fine cellular structures, to columnar dendrite with secondary dendrite arms and equiaxed structure at bottom, interface and top layers, respectively. The corrosion behavior of Inconel 625 alloy manufactured by WAAM was investigated by Wang et al. [22]. It was found that the microstructure at the top region was coarser due to the higher heat accumulation, which leads to the higher corrosion resistance in top region than that of other regions. Xu et al. [23] investigated the effect of oxide formation and heat treatment on the mechanical properties of WAAM Inconel 718. It was found that oxide formed during deposition was no effect on the mechanical properties. It was developed a protective oxide layer to prevent further oxidation forming inside the bulk. The strength of the heat-treated samples was lower in comparison to wrought alloy. Ravi et al. [24] investigated the mechanical and microstructural properties of Inconel 625 slab component fabricated by WAAM. The microstructures contained a columnar dendritic structure with the Laves phase and carbides. Kindermann et al. [25] carried out parametric study and heat treatments effects on CMT based WAAM of Inconel 718 alloy. The dimensions of the intermetallic phases like Laves phase and carbide got reduced with the increase of travel speed, whereas hardness of the deposited material got enhanced. Kumar and Maji [26] investigated the microstructure and chemical composition of bimetallic structure of Inconel 625 and stainless steel 304L using double wire arc additive manufacturing. It was found that the microstructure pure Inconel 625 was columnar dendrites. Wang et al. [27] concluded that the microstructure of Inconel 625 fabricated by CMT based WAAM assisted with magnetic field got refined due to the stirring and convection induced elemental diffusion. Chintala et al. [28] investigated the microstructure of thick slab wall component of Inconel 625 deposited through WAAM. The microstructures at the near substrate, layer band, and topmost region is cellular structure, columnar structure and equiaxed with a dendritic structure. Kumar [29] investigated the mechanical properties and microstructures of WAAM similar and dissimilar materials namely Stainless steels and Inconel 625 using tensile testing, microhardness tests

and fracture morphology of deposited thin wall geometry of Inconel 625 considering different parameters settings.

There are lot of work on Inconel 625 was done using laser-added and plasma-added additive manufacturing processes. The limited literature work focused on Inconel alloy modelling and manufacturing using WAAM. There are various advantages for WAAM over laser-added and plasma-added additive manufacturing processes, in terms of the capital expense of machines, high deposition rate, suitable for large and complex geometry, required low material cost, etc. Furthermore, no studies emphasize the optimization of input process parameters for deposition of single layer geometry of Inconel 625 using WAAM technique. Optimization of input process parameters of a WAAM technique is essential because it straightforwardly improves the deposition quality and quantity which thusly upgrades the usefulness of expensive material cost, reduced material wastages, and enhances productivity. The reported literatures work shows the microstructure of WAAM produced components fluctuated from substrate region to top region. Furthermore, no literature work focused on the anisotropy behaviour of tensile properties due to layer orientation at various angle. The microstructure advancement of WAAM component producing during the thermal cycles into the successive layer orientation and their connection with mechanical properties did not be additionally discussed.

In this paper three wall component of Inconel 625 was fabricated through GMAW based WAAM. The optimal set of process parameter for deposition of uniform single layer was selected through response surface methodology (RSM) and experimental data obtained through the Box–Behnken experimental design. At optimal process parameters, wall components were deposited and investigate the influence of layer orientation on the mechanical properties of Inconel 625 alloy into the three distinct directions as for the deposition layer i.e., transversal at 90° angle (T), longitudinal at 0° angle (L), and diagonal direction at 45° angle (D). The microstructural characterization and chemical compositional analysis were done using SEM with EDS to relate the specific microstructural features of Inconel 625 super alloy to the mechanical properties.

2 Experimental Procedure

2.1 WAAM Experimental Setup, Materials, and Methods

WAAM technique mainly consisted of two units, a heat source to melt the wire materials with an automated 3-axis stage machine (i.e. CNC machine or industrial robotic arm). The developed WAAM technology was good for fabricating the high-value parts in terms of productivity,

cost-competitiveness, and energy efficiency. CNC machine or industrial robotic arm based WAAM technology was not economical to access the technology for the small and medium industry due to the high cost of the CNC or industrial robotic arm. Therefore, with the help of open-source 3D movement package a 3D metal printer was developed for WAAM process shown in Fig. 1a.

The experimental setup mainly consisted of gas metal arc welding (GMAW) machine (MODEL No.: MIG 251; Make: Tornado) and the movement of the GMAW torch along Y and Z axis was controlled by a motorized 3-axis stage commanded by computer operated microcontroller. The deposition wire material is Inconel 625 of diameter 1 mm and chemical compositions are given in Table 1. Mild steel substrates of dimensions $130 \times 60 \times 10 \text{ mm}^3$ was used for the deposition of Inconel 625 wire material. The substrates were fixed on the moving stage in X-axis and the deposition torch was perpendicular to substrate. Before deposition the substrates were grinded using a surface grinder then it was cleaned in acetone and dried into the air to removed rust particles. Argon (Ar) gas was utilized as the shielding gas in all the experiments and the flow rat of

shielding gas was controlled manually by adjusting the cylinder tank valve meter.

The experimental work was divided into two-phases to study the effects of WAAM process parameters on mechanical and microstructural properties. Initially single layer geometry was deposited on substrate to observe the effect of input process parameters on single layer geometry measured in terms of bead width (BW) and bead height (BH) as shown in Fig. 1b. In second experimental case, multi-layer wall of Inconel 625 was deposited at optimal layer geometry.

2.2 Design of Experiments

At the starting of the experiment based on the broad literature survey and trial and error experimental observation four major response factors with three-level were selected as WAAM process parameters that significant effect on layer geometry, i.e., bead width (BW), bead Height (BH), bead cross-sectional area (BA), and additive efficiency (AE) as shown in Fig. 1a. The BA was estimated from the optical microscopy images of the deposited bead cross-sections through image processing technique utilizing the ImageJ software [29–31]. Additive efficiency was expressed as the volume material deposited per unit heat energy input, and calculated as the ratio of volumetric deposition rate to the power input. The power input ($P_{\text{net}} = \eta IV$, where η is the efficiency of the heat source, I is the current, V is the voltage) increased with the increase in voltage, resulted in increase in the amount of heat generated and consequently increased the melting rate [31, 33]. The GMAW power source set value was used to calculate the heat input keeping current constant for each condition. Volumetric deposition rate was calculated by weight difference measurement of inertial weight of substrate to final weight after deposition. The major response factors are voltage (V), wire feed rate (F), travel speed (S), and argon flow rate (G) [31, 32]. To investigate and optimize the main effects, quadratic effects and interaction effects of the independent variables on bead geometry modelling a four-factor, three-level Box–Behnken design (BBD) was used [31]. If K is a number of factors and a_0 is the number of centre points then the total number of experiments (N) to be conducted as according to Box–Behnken can be calculated by the following relation as given in equation $N = 2k(k - 1) + a_0$. The BBD of the experimental conditions are shown in Table 10 in appendix. The major response factors and their levels are shown in Table 2.

The RSM models were validate through a separate set of experiments within the range of upper and lower limit. The

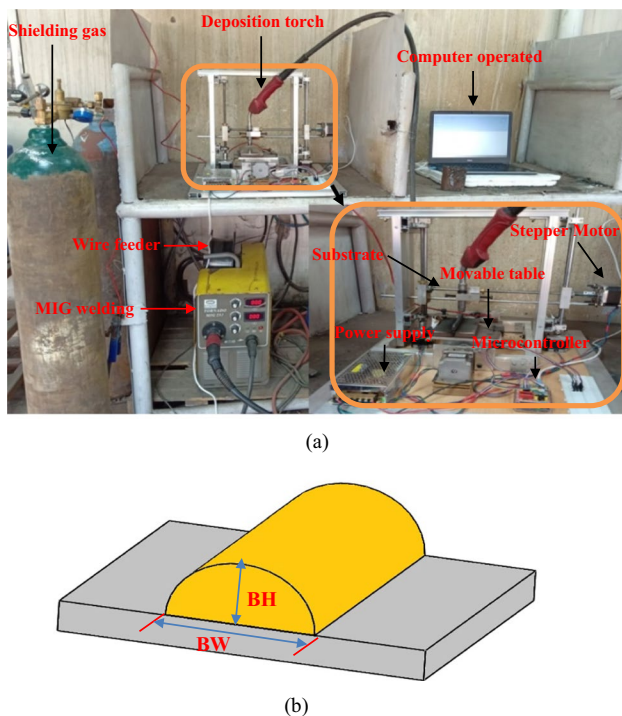


Fig. 1 a Experimental setup of wire arc additive manufacturing, and b Single layer geometry

Table 1 Chemical composition of wire electrode and substrate material in weight (%)

Grade	C	Mn	Si	P	S	Cr	Mo	Ni	N	Fe	Nb	Ti	Al	Co
Inconel 625	0.10	0.5	0.5	0.015	0.015	20–23	8–10	58–64		5	3.15–4.15	0.4	0.4	1
Mild Steel	0.14	0.56	0.30	0.045	0.045	–	–	–	–	Bal	–	–	–	–

Table 2 Input variables and their ranges

SL. no.	Input process parameters (unit)	Symbols	Minimum value	Mid value	Maximum Value
			- 1	0	+ 1
1	Voltage (Volt)	<i>V</i>	18	23	28
2	Wire feed rate (m/min)	<i>F</i>	4	6	8
3	Travel speed (mm/min)	<i>S</i>	150	200	250
4	Argon flow rate (lpm)	<i>G</i>	12	16	20

ten set of test data is shown in Table 3. The predicted value of RSM models were compared with the actual values of layer geometry obtained through experimentation. For better visualization of the test data mean absolute percentage error (MAPE) were calculated for all the developed RSM models i.e. 7.28, 8.29, 7.08, and 4.05 for BW, BH, BA, and AE, respectively. It was found that the MAPE errors were less than 9% for all the RSM models, which shows that the developed RSM models were adequate and good enough for predicting the bead layers.

The dependent variables for the single layer modelling are BW, BH, and BA. Single layer geometry was estimated from the optical macrographs of the bead cross-section utilizing ImageJ software. All responses were fitted to an RSM model in the form of second order quadratic model and the adequacy of RSM model for single layer was verified by ANOVA, lack of fit and coefficient of determination (R^2) tests. The experimental data were used as training data, and statistical software Minitab 17 was utilized to obtain response models. The equations resulted in empirical models that relate the measured response to the independent variables of the experiment. The model is expressed as the following Eq. 1.

$$y = \beta_0 + \sum_{i=1}^k \beta_i x_i + \sum_{i=1}^k \beta_{ii} x_i^2 + \sum_{i=1}^{k-1} \sum_{j=2}^k \beta_{ij} x_i x_j \tag{1}$$

where y is the response, the β parameters are called the regression coefficients; x_i is the number of independent variables. The developed RSM-models of BW, BH, BA, and AE are given in Eq. 2, 3, 4 and 5 respectively.

$$\begin{aligned}
 BW = & 11.33 - 0.567V + 1.104F - 0.0377S \\
 & - 0.074G + 0.03468V^2 + 0.0515F^2 \\
 & + 0.000143S^2 + 0.01341G^2 \\
 & - 0.0190VF - 0.002220VS - 0.01119VG \\
 & + 0.00017FS - 0.0648FG + 0.000906SG
 \end{aligned} \tag{2}$$

$$\begin{aligned}
 BH = & 15.47 - 1.162V + 0.265F - 0.0296S \\
 & + 0.085G + 0.01839V^2 + 0.0751F^2 \\
 & + 0.000036S^2 - 0.01087G^2 + 0.0118VF \\
 & + 0.000870VS + 0.01262VG \\
 & - 0.00266FS - 0.0341FG + 0.000500SG
 \end{aligned} \tag{3}$$

$$\begin{aligned}
 BA = & 24.9 - 4.32V + 3.62F - 0.062S \\
 & + 2.36G + 0.1230V^2 + 0.296F^2 \\
 & + 0.000215S^2 - 0.0602G^2 \\
 & + 0.0739VF - 0.00305VS \\
 & - 0.0033VG - 0.01084FS \\
 & - 0.2914FG + 0.00435SG
 \end{aligned} \tag{4}$$

$$\begin{aligned}
 AE = & 46.9 - 5.56V + 1.89F - 0.096S + 2.55G \\
 & + 0.1128V^2 + 0.367F^2 - 0.000010S^2 \\
 & - 0.0754G^2 + 0.0194VF + 0.00208VS \\
 & + 0.0315VG + 0.00411FS \\
 & - 0.3312FG + 0.00269SG
 \end{aligned} \tag{5}$$

The statistical results of analysis of variance (ANOVA) and lack of fit tests of the developed RSM models were revealed in Table 4. An ANOVA test is a statistical method to find out that the survey or experiment results are significant. The F-statistic is simply a ratio of two variances. In the ANOVA test of the responses (i.e. BH, BW, BA, and AE), the probability values (P) of F-statistic of the developed models were larger than the tabulated values at 95% confidence level and the P-value of the developed models were found to be less than 5%. As a consequence, it was found that all the P-values of the developed RSM models accomplished the fitted quadratic model well ($P < 0.05$). In this study, the coefficients of determination (R^2) values for the responses BH, BW, BA, and AE were 0.905, 0.865, 0.94, and 0.873 respectively.

Table 3 Experimental test data for validation of the RSM models of layer geometry

SL. no.	Process parameters				Layer Geometric parameters							
	V (volt)		F (m/min)	S (mm/min)	Experimental values			Predicated Values				
	G (lpm)	BW (mm)	BH (mm)	BA (mm ²)	AE (mm ³ /kJ)	BW (mm)	BH (mm)	BA (mm ²)	AE (mm ³ /kJ)			
1	21	3	180	14	5.23	1.64	4.38	5.32	4.7	1.66	4.06	5.89
2	21	7	220	14	5.14	2.31	9.72	14.18	5.55	2.54	10.29	13.89
3	26	3	180	14	7.37	2.2	8.57	9.08	6.95	2.02	9.48	9.51
4	26	7	220	14	6.8	3.51	15.64	18.34	6.97	3.3	16.59	17.89
5	21	3	180	18	4.83	1.33	6.11	6.96	5.06	1.62	5.14	6.50
6	21	7	220	18	5.55	1.89	8.18	10.48	5.01	2.04	7.41	11.02
7	26	3	180	18	6.34	2.06	11.1	10.34	7.09	2.23	10.5	10.52
8	26	7	220	18	6.51	3.32	13.44	15.28	6.21	3.05	13.64	14.94
9	21	7	180	14	6.81	3.05	12.82	13.82	6.08	2.89	12.48	13.31
10	26	3	220	18	5.94	2.41	9.54	11.04	6.23	2.56	10.13	11.26

Table 4 Analysis of variance (ANOVA) (a) BW, (b) BH, (c) BA, and (d) AE

Source	DF	Adj SS	Adj MS	F	P
(a) BW					
Regression	14	92.464	6.6046	26.62	0.000
Linear	4	78.621	19.6552	79.21	0.000
Square	4	8.272	2.0679	8.33	0.000
Interaction	6	5.572	0.9286	3.74	0.005
Residual Error	39	9.677	0.2481		
Lack-of-Fit	10	9.079	0.9079	44.04	0.000
Pure Error	29	0.598	0.0206		
Total	53	102.141			
(b) BH					
Regression	14	31.9054	2.2790	17.89	0.000
Linear	4	25.4439	6.3610	49.94	0.000
Square	4	4.2214	1.0554	8.29	0.000
Interaction	6	2.2401	0.3734	2.93	0.019
Residual Error	39	4.9678	0.1274		
Lack-of-Fit	10	4.5594	0.4559	32.37	0.000
Pure Error	29	0.4084	0.0141		
Total	53	36.8732			
(c) BA					
Regression	14	1577.87	112.705	44.56	0.000
Linear	4	1355.94	338.985	134.04	0.000
Square	4	153.95	38.489	15.22	0.000
Interaction	6	67.98	11.330	4.48	0.002
Residual Error	39	98.63	2.529		
Lack-of-Fit	10	88.17	8.817	24.43	0.000
Pure Error	29	10.47	0.361		
Total	53	1676.51			
(d) AE					
Regression	14	1126.43	80.459	19.20	0.000
Linear	4	900.92	225.230	53.74	0.000
Square	4	160.03	40.009	9.55	0.000
Interaction	6	65.47	10.912	2.60	0.032
Residual Error	39	163.45	4.191		
Lack-of-Fit	10	149.92	14.992	32.14	0.000
Pure Error	29	13.53	0.467		
Total	53	1290.88			

2.3 Parametric Effects on Bead Geometry

The developed RSM models were used to plot three-dimensional response surface plots as shown in Fig. 2. Response surface plots are very useful for considering the interaction effects between two factors and for seeing how the impact of one factor will be affected by the adjustment in the level of another factor. It was observed from Fig. 2a–c that layer geometry increases with increases of voltage and wire feed rate and layer geometry decreases with increases of travel speed and gas flow rate. The

Fig. 2 Response surface plots for **a** BW, **b** BH, **c** BA, and **d** AE

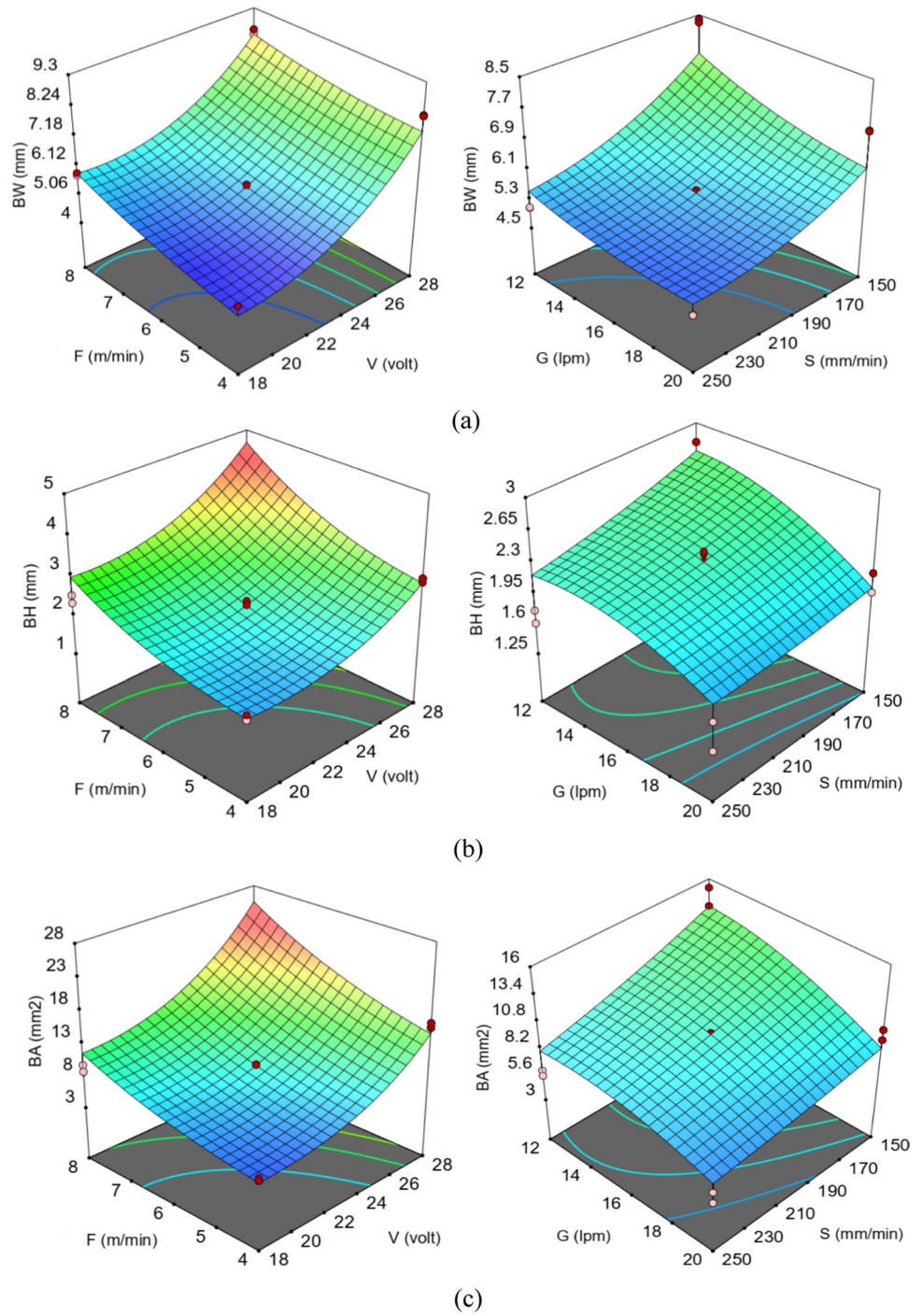
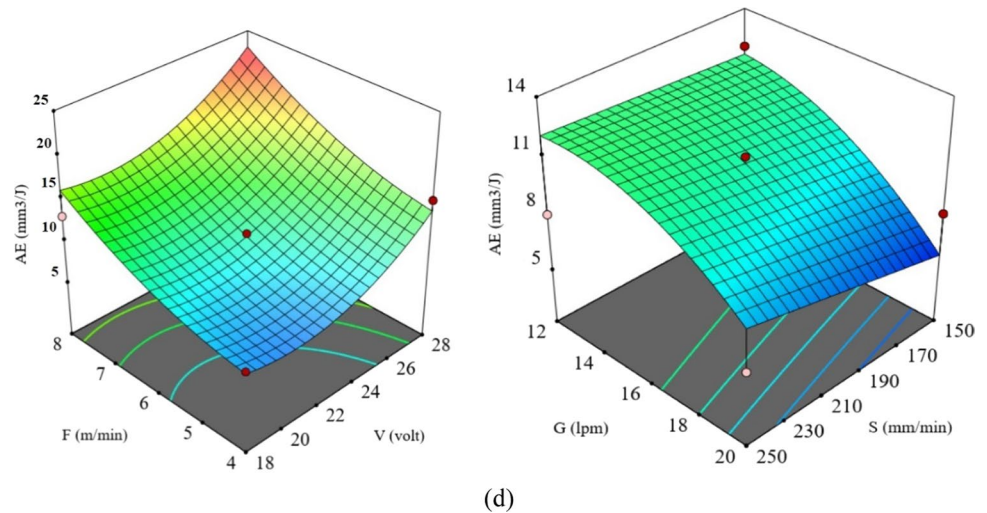


Fig. 2 (continued)



voltage, wire feed rate and travel speed have major significant role in affecting layer geometry. The layer geometry decreases with increases of travel speed, as shown in Fig. 2a–c. The reason behind is that the material deposition rate per unit length of the layer is reduced due to higher travel speed for a given wire feed rate. The higher travel speed decreases the heat input per unit length, resulting in less amount of wire material melt and deposited. However, bead layer increases with increases of voltage and wire feed rate. The reason behind is that with increases of voltage power input increases which increases the melt off rate of wire material due to higher amount of heat is generated at the tip of the wire electrode. Shielding gas has lesser significant on layer geometry comparison to other process parameter but with decreasing the flow rate there is a chance of contamination from surrounding air.

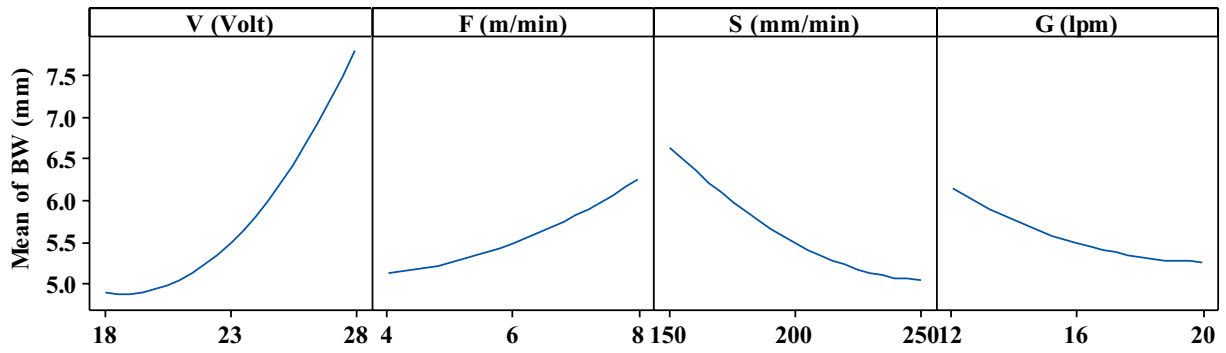
As voltage increases, heat input increasing the AE and temperature of molten metal as shown in Fig. 2d. Due to this, the molten metal will be at high temperatures. As the temperature of molten metal increases, both surface tension and viscosity decrease, which determine the shape of the beads [34, 35]. Molten metal has a low surface tension and viscosity, allowing it to spread out due to high heat input and causes the continuous increase of the layer width. Similarly, with increases of travel speed makes it possible for molten metal to be deposited over a wider area for the same amount of metal. Similarly, increases of wire feed rate shows a reduction in heat input if other parameters remain the same. The temperature of the molten metal decreases as more material is melted using the same amount of energy. Due to its lower temperature, molten metal solidifies faster, preventing it from spreading. Therefore, the layer height is increasing greater in comparison to layer width as per shown in Fig. 3a, b. Therefore, optimal process parameters required to deposited uniform single layer geometry for multi-bead deposition.

The main effect plot shows that voltage, wire feed rate, travel speed, and gas flow rate are directly influenced the bead geometry as shown in Fig. 3.

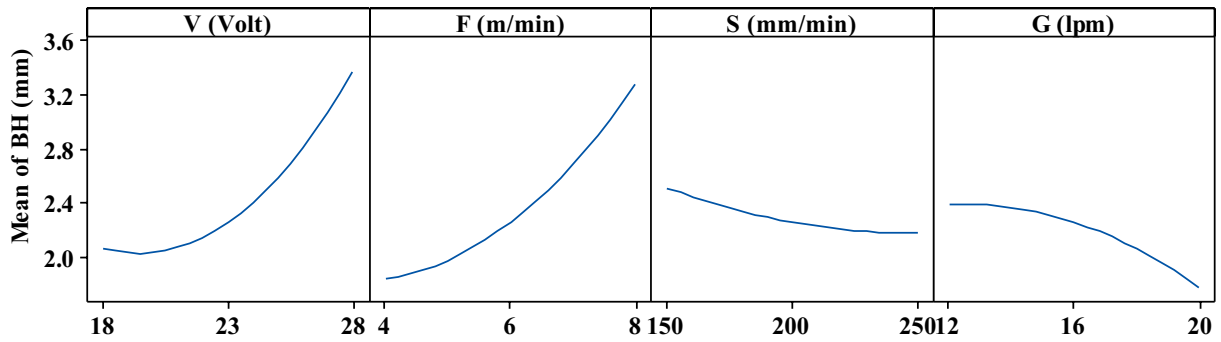
Minitab 17 software was utilized to run the desirability function optimizer module in order to optimize the input parameters based on the effects of the input parameters on all three responses. Response variable BW, BH, BA and Q converted into individual desirability scale d_1 , d_2 , d_3 , and d_4 respectively. Constraints for the entire response variable were set to be maximization and minimization. All the response variable was provided equal weightage and importance. The optimization plots result for BW, BH, BA and AE were tabulated in Table 5.

Figure 4 shows experimental validation of the optimal settings in case of maximum and minimum layer geometry deposited at the optimal layer geometry sizes from the response optimization. SEM images were analysed through ImageJ using the geometric characteristics of experimentally deposited layers. The optimal layer geometry sizes with absolute percentage errors are shown in Table 6.

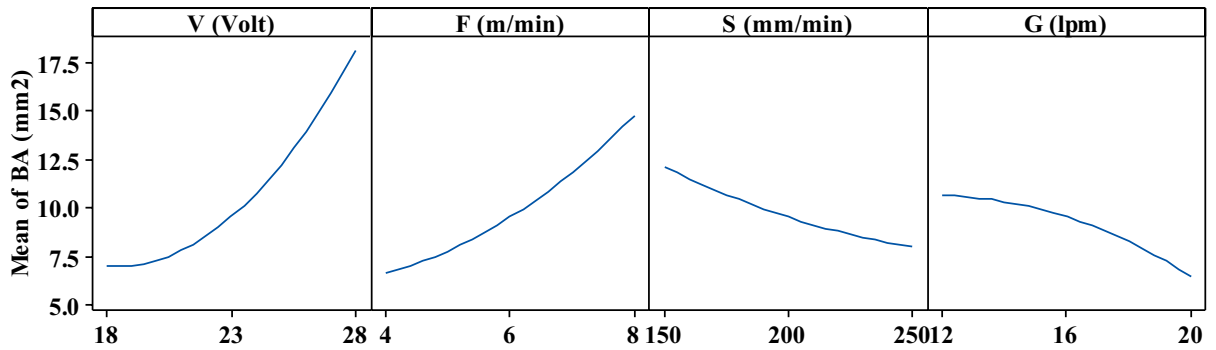
It was clearly observed that the process parameters were affected the bead geometry characteristics. The layer geometry was adjusted to its suitable size by using the response surface optimizer module. In case of multibead multilayer (MBML) deposition maximum bead geometry optimization condition was suitable but in case of thin wall deposition targeted bead geometry condition was suitable. MBML methods are used to build three-dimensional parts by depositing material in the form of beads with fixed sizes in both horizontal and vertical directions. The manufacturing of a wall-type structure is achieved through the deposition of single-bead multilayers (SBML) only in vertical direction [31]. For this reason, to maintain the thickness of a thin wall and to require less post-processing in the part manufactured through WAAM process targeted bead geometry should be higher bead height (BH) and lower bead width (BW).



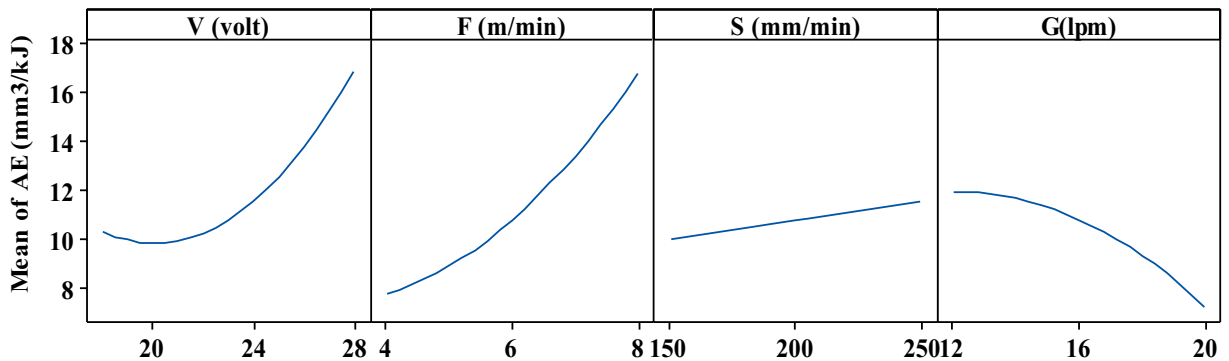
(a)



(b)



(c)



(d)

Fig. 3 Main effects plots for a BW, b BH, c BA, and d AE

Table 5 Optimum bead sizes for wire arc additive deposition

Optimization cases	Responses				Input parameters			
	BW (mm)	BH (mm)	BA (mm ²)	AE (mm ³ /kJ)	V (Volt)	F (m/min)	S (mm/min)	G (lpm)
Maximization	11.65	5.05	32.98	25.04	28	8	150	12
Minimization	4.72	1.24	4.72	5.38	19.41	5.05	216.66	19.91

Fig. 4 Deposited weld bead geometry **a** At minimum and maximum process parameters, and **b** SEM image of bead geometry at maximum process parameters

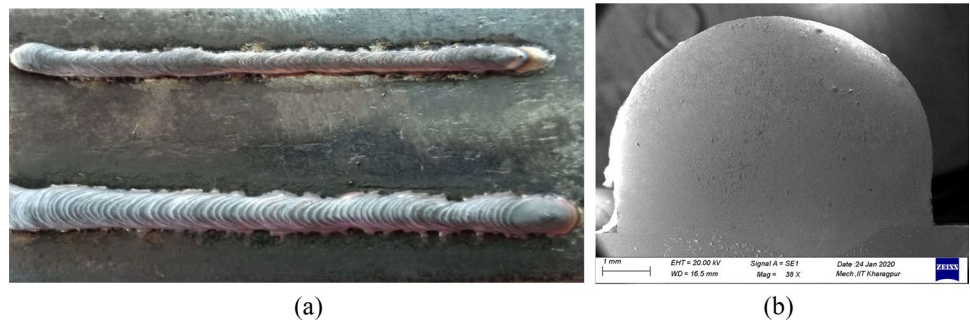


Table 6 Theoretical and experimental comparison of optimal bead sizes

Bead geometry parameters	Maximum			Minimum		
	Predicated values	Experimental value	Error %	Predicated values	Experimental value	Error %
BW (mm)	11.65	11.89	2.06	4.72	4.82	1.94
BH (mm)	5.05	5.17	2.42	1.24	1.27	2.42
BA (mm ²)	32.98	34.10	3.39	4.72	4.83	2.33
AE (mm ³ /kJ)	25.04	24.14	3.09	5.38	6.06	3.73

Table 7 Process parameters used for WAAM deposition

Parameters with units	Values
Voltage (Volt)	28
Wire feed rate (m/min)	6
Travel speed (mm/min)	250
Gas flow rate (lpm)	16

Therefor to build a thin wall of Inconel 625 the suitable process parameters was obtained through response surface optimizer module.

3 Wall Deposition and Specimen Preparation

The wall geometry of 65 layers was fabricated through WAAM process using Inconel 625 alloy. The optimal set of input parameters for deposition of wall geometry was obtained from the response surface optimizer module is presented in Table 7.

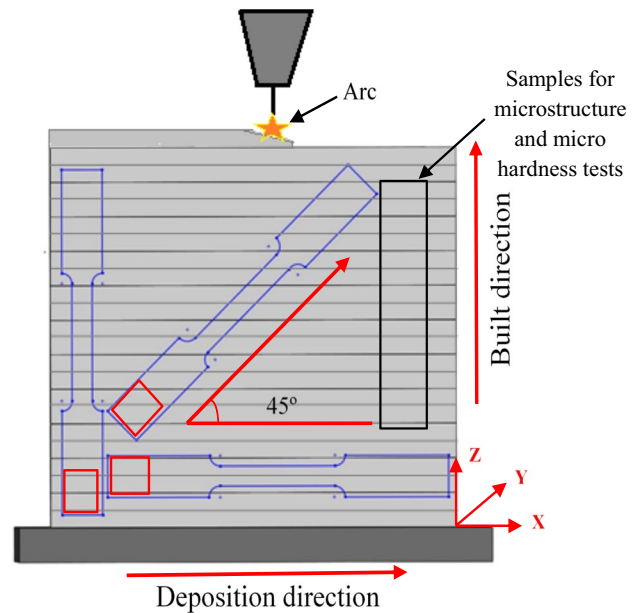


Fig. 5 The sample positions

3.1 Microstructural and Chemical Test Sample

The microstructures and elemental composition of the as-deposited component were investigated. Samples for testing were sectioned as shown in Fig. 5. Both ends (10 mm) of each wall were cut off and removed. The built wall was subsequently milled into a thickness of 4 mm using a vertical CNC milling machine. Samples for microstructure, micro hardness tests, SEM with EDS were taken from the middle part of the wall and testing was done through out the wall i.e. from bottom to top. The samples were grinded with different grit size (i.e. starting from 100 to 1800 grit) of emery papers and polished by diamond paste of different sizes, i.e., 3 μm , 1 μm , 0.25 μm , and followed by colloidal silica (SiO_2) suspension. The microstructures of the test pieces were investigated using optical microscope (Model: Leica DMLM, Make: Leica (Made in Germany)) and Scanning Electron Microscope (SEM) with EDS (ZEISS EVO 18). The grinded samples were etched to clarify the grain boundaries in the materials. In a mixed solution of 80 ml 96% ethyl alcohol, 40 ml 32% hydrochloric acid and copper (II) chloride 2 g was used for chemically etching of samples.

3.2 Mechanical and Fractographic Sample

Tensile tests were conducted to investigate the joint strength and tensile strength of the built wall. Three specimens for each distinct direction were sectioned by wire cut electrical discharge machining (WEDM) from deposited wall shown in Fig. 5a. The tensile tests were done at room temperature using a Tinius Olsen/ H25 KT universal testing machine at a crosshead velocity of 1 mm/min. Samples for micro hardness test were sectioned from the middle part of the deposited wall and hardness was measured from bottom to top of the deposited wall shown in Fig. 5a. The micro-hardness of the deposited wall was analysed along the direction of deposition. The micro-hardness of the wall samples was measured at the three different regions i.e., at bottom, middle and top the wall using Vickers micro-hardness testing machine (Model: UHL VMHT) at a weight of 500 gm for a dwell period of 15 s at intervals of 0.5 mm.

Table 8 Tensile strength variation in different direction

Samples	No. of Sample	YS	UTS	Elongation (%)
Longitudinal direction (L)	L-1	541	809	64.1
	L-2	495	785	66.8
	L-3	491	779	64.5
Transversal direction (T)	T-1	470	730	62.4
	T-2	482	774	64
Diagonal direction (D)	D-1	406	701	79.2
	D-2	397	637	72.3

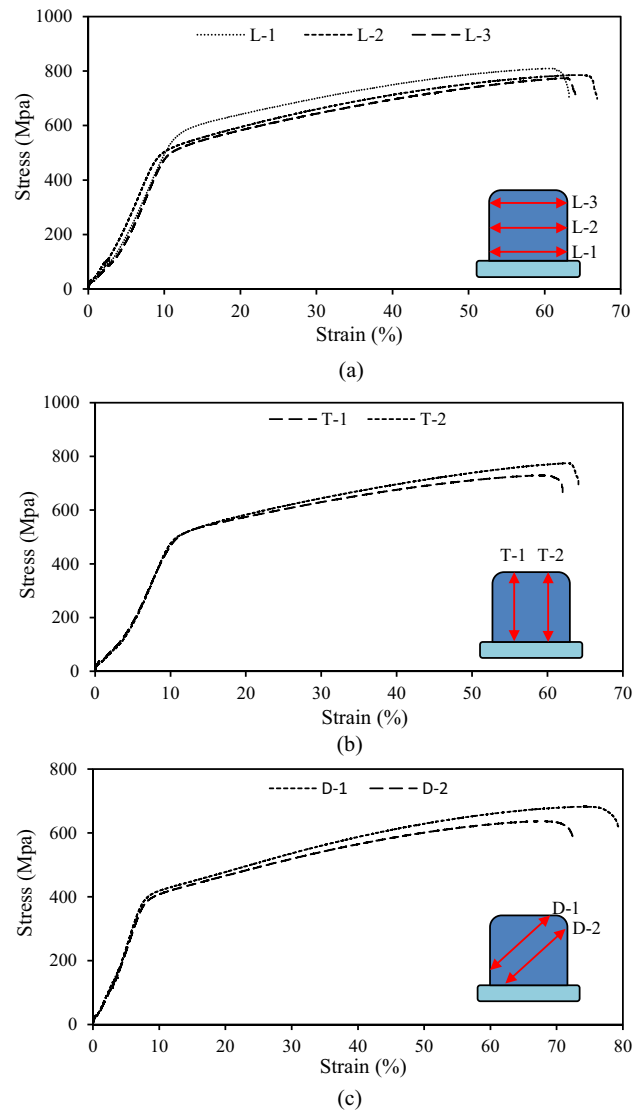


Fig. 6 Stress vs Strain graphs **a** Longitudinal direction (L), **b** Transversal direction (T), and **c** Diagonal direction (D)

After the tensile tests for fractographic analysis specimens were prepared from the fractured tensile specimen. The fractured surface was analysed with SEM with EDS to investigate the mode of failure.

4 Results and Discussion

4.1 Mechanical Properties Analysis

The yield strength (YS), ultimate tensile strength (UTS) and the percent of uniform elongation were measured for all the tensile specimens along in the build direction (T), deposition direction (L) and diagonal direction (D). The tensile properties of the deposited wall materials are listed in Table 8.

Fig. 7 Tensile strength and elongation variation in different direction

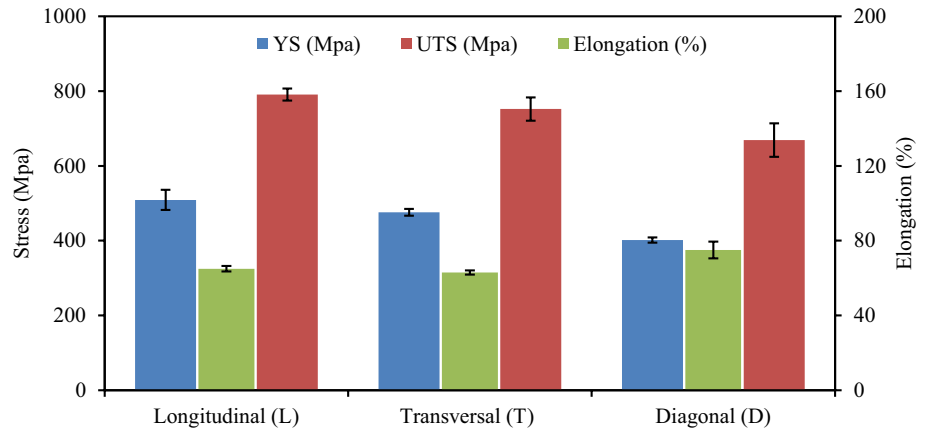


Table 9 Inconel 625 tensile properties from literature review classified according to the type of the process

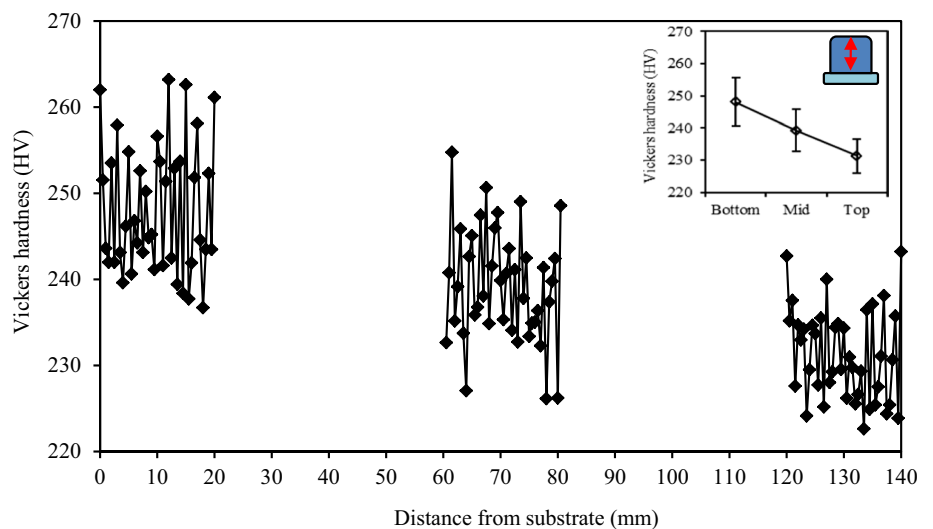
Process	Heat source	Specimen orientation	YS (Mpa)	UTS (Mpa)	Elongation (%)	Microhardness (HV)	Reference
WAAM	GMAW	T	476	752	63.2	236–252	Present study
		L	509	791	65.13		
		D	401	669	75.75		
WAAM	GTAW	T	–	684	40.13	240–270	Wang et al. [17]
		L	–	722	42.27		
L-PBF	L-PBF	T	516	893	54		Hack et al. [18]
		L	549	958	46		
WAAM	CMT-GMAW	T	376	628	43	246–264	Yangfan et al. [21]
		L	392	672	46.5		
Casting	–	–	456–487	825–849	47–49	–	Gupta et al. [36]

Figure 6 shows the engineering stress–strain curves of the specimens deposited through WAAM. Figure 6a shows the YS and UTS value gradually decreases from the bottom to top region of deposited metal. The near-substrate region has the highest tensile strength and the average YS, UTS

and elongation (%) value of the three places are 509Mpa, 791Mpa and 65.13% respectively.

The graphical comparison of the tensile properties i.e. YS, UTS and elongation (%) of the tested samples in three different orientations (T, L and D) were represented by

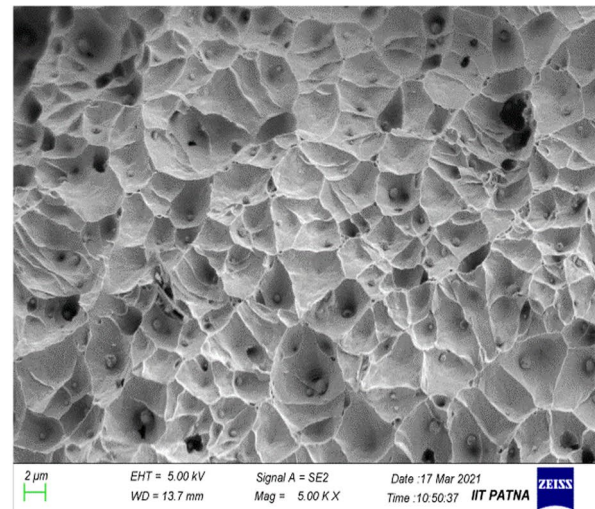
Fig. 8 Micro hardness variation across the built direction



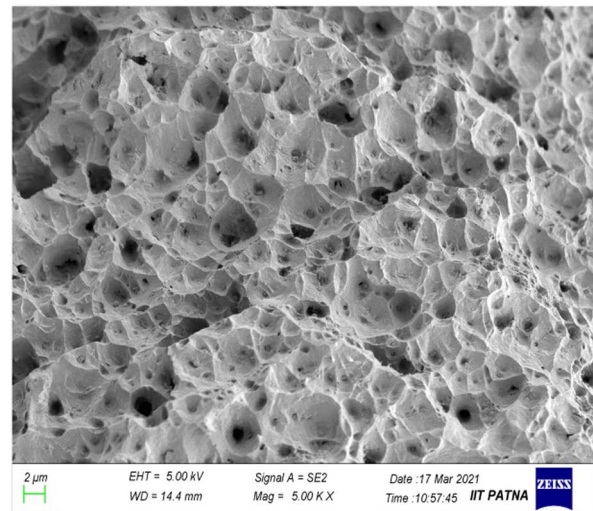
histograms as shown in Fig. 7. The trends of graph of tensile properties clearly observed an anisotropic behaviour of WAAM deposited Inconel 625. It was observed that the average values of YS, UTS and elongation (%) (509 Mpa, 791 Mpa and 65.13%) of L direction sample, (476 Mpa, 752 Mpa and 63.2%) of T direction sample, and (401 Mpa, 669 Mpa, and 75.75%) of D direction sample were found to be anisotropy in different direction. The YS, UTS, and EL of the L-direction were better than the other two directions shown in Fig. 7. Due to layer-by-layer build path in WAAM process directional thermal gradients produced. The microstructure of component was fabricated by WAAM exhibit anisotropic properties because of generation of directional thermal gradients. The anisotropy exists in the mechanical property of the fabricated wall using WAAM process. The grain boundary strengthen is different in different direction due to anisotropy. The anisotropy in mechanical properties, the tensile strength is different along the deposition and builds directions.

The tensile properties from literature review classified according to the type of the different additive manufacturing (AM) process and casting process are listed in Table 9. It was found that the previous stayed on mechanical properties of Inconel 625 alloy was mainly focused on the L and T specimens' direction. Further no data was reported on D specimens' direction. The comparison of the mechanical properties results of the present study with the results of the previous reported studies on the Inconel 625 alloy deposited through different AM process, it was observed that, anisotropic properties exhibit between T and L direction and from present study it was also evident that the WAAM deposited metal can exhibit anisotropic properties with changes of layer orientations.

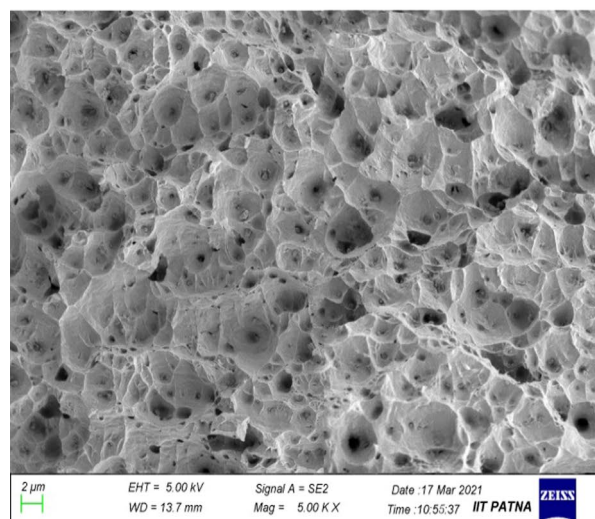
Figure 8 depicts the results of a micro-hardness test for the wall samples across the built direction. The micro-hardness test of as-deposited wall was analysed at three regions i.e. top, middle and bottom region. In the bottom region near to the substrate the flow of heat was take place in all three mode of heat transfer. The rapid flow of heat during solidification inculation takes place several places resulting in fine microstructure. Due to fine microstructure the micro-hardness is higher at the bottom region. After several layers deposition above the bottom region temperature gradient becomes small and the cooling rate becomes low due to heat accumulation. Therefore, the microstructure of middle region forms fine, with some amount of secondary dendrite that reduces the micro-hardness in compared to bottom. In the top region there was no further melting take place at the upper layer. Hence the temperature gradient becomes much smaller and form coarser microstructure that reduces the micro-hardness in compared to bottom and intermediate layers as per shown in Fig. 8.



(a)



(b)



(c)

Fig. 9 Fracture morphologies of **a** Longitudinal (L), **b** Transversal (T), and **c** Diagonal direction (D) samples

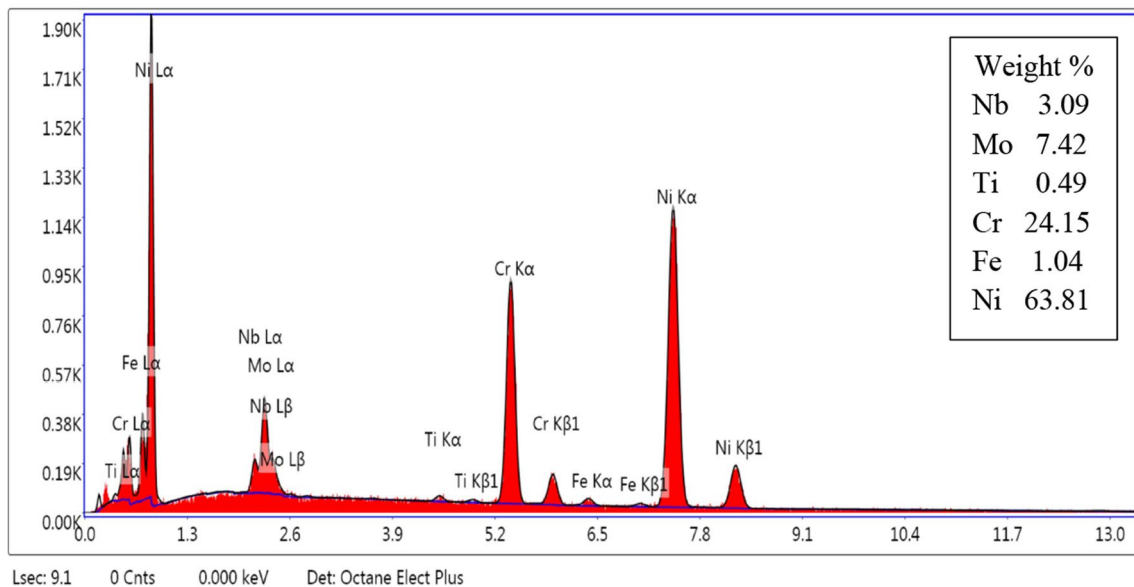
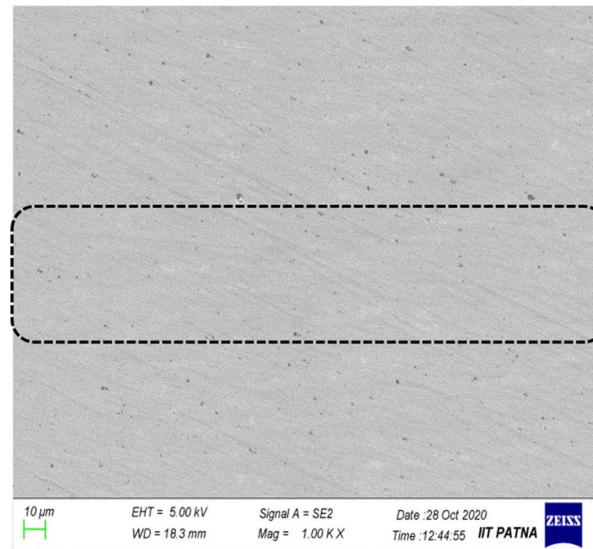


Fig. 10 SEM image of wall sample with EDS

4.2 Fracture Morphology and Microstructure

The fracture morphologies of tensile samples were analysed by SEM as shown in Fig. 9. The fracture of tensile specimens took place within the gauge length. The fracture morphologies of the tensile specimens appeared with sharp tearing edges and large number of fine dimpled surfaces in all the tested specimens, independently from

specimen orientation that indicated the ductile failure as shown in Fig. 9.

Figure 10 shows the higher magnification SEM image of Inconel 625 wall sample with EDS analysis. WAAM is a welding-based AM technique and during deposition each layer affected by continuous changing of thermal cycles. Typically, the microstructure of WAAM Inconel 625 alloy

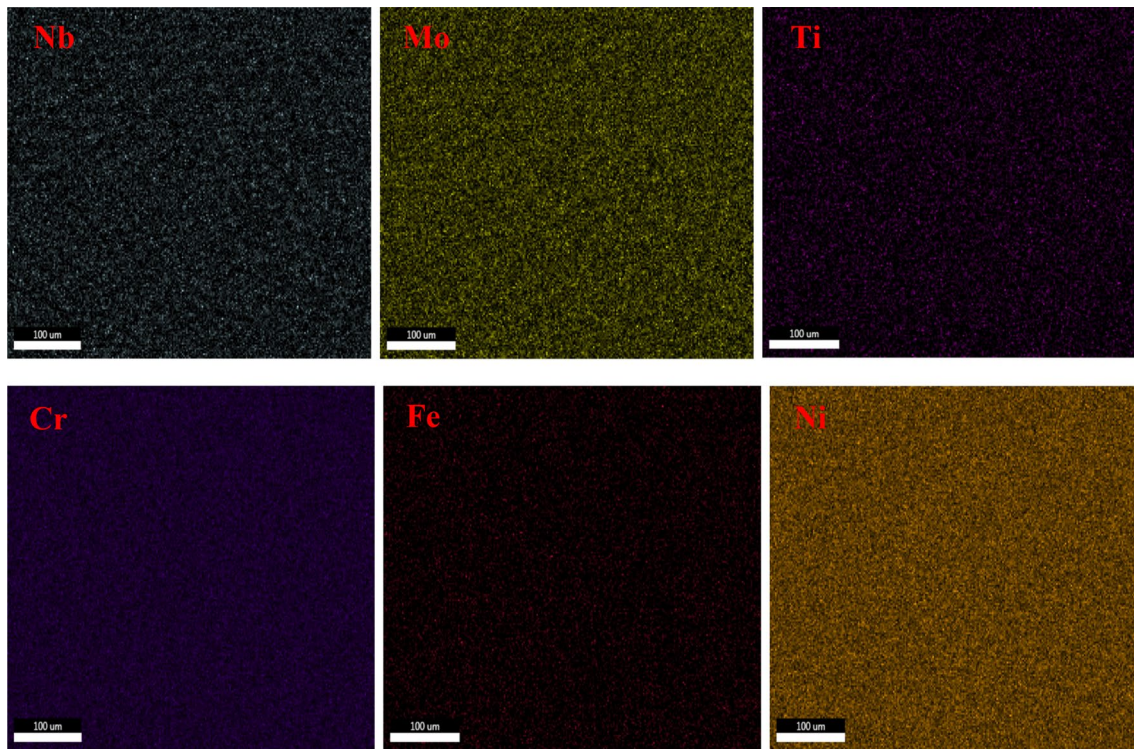


Fig. 11 SEM micrograph and EDS elemental maps of Nb, Mo, Ti, Cr, Fe and Ni in Inconel 625 wall sample

reveals columnar dendritic structure, growing epitaxially along the deposition direction as shown in Fig. 10 [20].

EDS elemental mapping of Inconel 625 wall sample is shown in Fig. 11. The EDS elemental mapping depicts the scattering of all the major alloying elements of Inconel 625.

5 Conclusions

Deposition geometry model was developed based on response surface method using experimental data collected following the Box–Behnken design of experiments method to predict width, height, and cross-sectional area for single track deposition of Inconel 625 by WAAM. The developed model of deposition geometry was expressed as a function of the input parameters, i.e., voltage, wire feed rate, torch travel speed and gas flow rate. The models built were verified by a separate set of experimental data within the ranges of design matrix and found to provide satisfactory prediction accuracy. All the responses were found to increase with the increase of voltage, and wire feed rate and decreased with increase of torch travel speed

and gas flow rate. At suitable process parameters obtained through response surface analysis the wall of Inconel 625 was deposited and investigated the mechanical properties. The tensile properties of deposition direction were better than the other two directions. Also, the tensile strength of deposition direction was highest near-substrate region and successively decreases along built direction. The microhardness was highest at the bottom region successively decreases along built direction. The microstructures of Inconel 625 were composed of columnar dendritic structure. The fracture morphologies of the tensile specimens appeared with sharp tearing edges and large number of fine dimpled surfaces indicated the ductile failure with good layer bonding. Scopes for future study on possible ways to reduce anisotropy and inhomogeneity in properties of the WAAM parts are also mentioned.

Appendix

See Table 10.

Table 10 The BBD of the experimental conditions with heat input and energy density

SL. no.	Process parameters				Bead Geometric parameters			
	V (V)	F (m/min)	S (mm/min)	G (lpm)	BW (mm)	BH (mm)	BA (mm ²)	AE (mm ³ /kJ)
1	18	4	200	16	4.73	1.79	5.41	11.65
2	28	4	200	16	8.15	2.9	15.57	21.97
3	18	8	200	16	5.87	2.42	9.23	19.72
4	28	8	200	16	8.52	4.01	22.35	31.15
5	23	6	150	12	8.29	2.65	14.3	18.65
6	23	6	250	12	5.08	1.69	5.79	12.13
7	23	6	150	20	7.19	1.98	9.39	11.79
8	23	6	250	20	4.7	1.42	4.36	9.66
9	18	6	200	12	5.31	3.02	10.07	22.31
10	28	6	200	12	8.79	3.32	19.86	28.05
11	18	6	200	20	4.8	1.65	4.74	9.99
12	28	6	200	20	7.39	2.96	14.27	19.84
13	23	4	150	16	5.49	1.62	6.01	7.77
14	23	8	150	16	7.14	4.19	19.74	25.36
15	23	4	250	16	4.93	2.03	6.12	13.10
16	23	8	250	16	6.65	3.54	15.52	32.64
17	18	6	150	16	5.26	2.24	7.95	12.97
18	28	6	150	16	9.03	3.55	21.66	22.98
19	18	6	250	16	4.92	1.69	5.95	16.37
20	28	6	250	16	6.48	3.87	16.61	29.13
21	23	4	200	12	5.09	1.69	5.43	8.92
22	23	8	200	12	7.07	3.64	17.78	30.75
23	23	4	200	20	5.2	1.74	6.18	10.57
24	23	8	200	20	5.11	2.59	9.21	15.35
25	23	6	200	16	5.47	2.28	9.23	15.60
26	23	6	200	16	5.4	2.33	9.69	16.49
27	23	6	200	16	5.56	2.16	9.51	16.30

Acknowledgements The authors gratefully acknowledge the support of Mechanical Engineering Department of NIT Patna, TRTC Patna, CMERI Durgapur and IIT Patna for providing the experimental facilities for successful completion of this research work.

References

- Cao, Y., Zhu, S., Liang, X., & Wang, W. (2011). Overlapping model of beads and curve fitting of bead section for rapid manufacturing by robotic MAG welding process. *Robotics and Computer-Integrated Manufacturing*, 27, 641–645. <https://doi.org/10.1016/j.rcim.2010.11.002>
- Xiong, J., Zhang, G., Gao, H., & Wu, L. (2012). Modeling of bead section profile and overlapping beads with experimental validation for robotic GMAW-based rapid manufacturing. *Robotics and Computer-Integrated Manufacturing*, 29, 417–423. <https://doi.org/10.1016/j.rcim.2012.09.011>
- Ding, D., Pan, Z., Cuiuri, D., & Li, H. (2015). A multi-bead overlapping model for robotic wire and arc additive manufacturing. *Robotics and Computer-Integrated Manufacturing*, 31, 101–110. <https://doi.org/10.1016/j.rcim.2014.08.008>
- Kumar, N. P., Devarajan, P. K., Vendan, S. A., & Shanmugam, N. (2017). Prediction of bead geometry in cold metal transfer welding using back propagation neural network. *International Journal of Advanced Manufacturing Technology*, 93, 385–392. <https://doi.org/10.1007/s00170-016-9562-8>
- Youheng, F., Guilain, W., Haion, Z., & Liy, L. (2017). Optimization of surface appearance for wire and arc additive manufacturing of Bainite steel. *International Journal of Advanced Manufacturing Technology*, 91, 301–313. <https://doi.org/10.1007/s00170-016-9621-1>
- Sarathchandra, D. T., Davidson, M. J., & Visvanathan, G. (2020). Parameters effect on SS304 beads deposited by wire arc additive manufacturing. *Materials and Manufacturing Processes*, 3, 852–858. <https://doi.org/10.1080/10426914.2020.1743852>
- Dinovitzer, M., Chen, X., Laliberte, J., Huang, X., & Frei, H. (2019). Effect of wire and arc additive manufacturing (WAAM) process parameters on bead geometry and microstructure. *Additive Manufacturing*, 26, 138–146. <https://doi.org/10.1016/j.addma.2018.12.013>
- Bharat Kumar, C. H., & Anandakrishnan, V. (2019). Experimental investigations on the effect of wire arc additive manufacturing process parameters on the layer geometry of Inconel 825. *Materials Today: Proceedings*, 21, 622–627. <https://doi.org/10.1016/j.matpr.2019.06.727>
- Kumar, V., Mandal, A., Das, A. K., & Kumar, S. (2021). Parametric study and characterization of wire arc additive manufactured steel structures. *The International Journal of Advanced*

- Manufacturing Technology*, 115, 1723–1733. <https://doi.org/10.1007/s00170-021-07261-6>
10. Le, V. T., Mai, D. S., Doan, T. K., & Paris, H. (2021). Wire and arc additive manufacturing of 308L stainless steel components: Optimization of processing parameters and material properties. *Engineering Science and Technology, an International Journal*, 24(4), 1015–1026. <https://doi.org/10.1016/j.jestech.2021.01.009>
 11. Tonelli, L., Laghi, V., Palermo, M., Trombetti, T., & Ceschini, L. (2021). AA5083 (Al–Mg) plates produced by wire-and-arc additive manufacturing: Effect of specimen orientation on microstructure and tensile properties. *Progress in Additive Manufacturing*, 6(3), 479–494. <https://doi.org/10.1007/s40964-021-00189-z>
 12. Abdelall, E. S., Al-Dwairi, A. F., Ashour, E., & Eldakrouy, M. (2021). Experimental study of a novel layer deposition technique and its effect on anisotropic behavior of wire arc additively manufactured steel parts. *Progress in Additive Manufacturing*, 6(4), 871–879. <https://doi.org/10.1007/s40964-021-00201-6>
 13. Dinda, G. P., Dasgupta, A. K., & Mazumder, J. (2009). Laser aided direct metal deposition of Inconel 625 superalloy: Microstructural evolution and thermal stability. *Materials Science and Engineering*, 509, 98–104. <https://doi.org/10.1016/j.msea.2009.01.009>
 14. Xu, F. J., Lv, Y. H., Xu, B. S., Liu, Y. X., Shu, F. Y., & He, P. (2013). Effect of deposition strategy on the microstructure and mechanical properties of Inconel 625 superalloy fabricated by pulsed plasma arc deposition. *Materials and Design*, 45, 446–455. <https://doi.org/10.1016/j.matdes.2012.07.013>
 15. Xu, F., Lv, Y. H., Liu, Y., Shu, F., He, P., & Xu, B. (2013). Microstructural evolution and mechanical properties of inconel 625 alloy during pulsed plasma arc deposition process. *Journal of Materials Science & Technology*, 29(5), 480–488. <https://doi.org/10.1016/j.jmst.2013.02.010>
 16. Li, S., Wei, Q., Shi, Y., Zhu, Z., & Zhang, D. (2015). Microstructure characteristics of inconel 625 superalloy manufactured by selective laser melting. *Journal of Materials Science & Technology*, 31, 946–952. <https://doi.org/10.1016/j.jmst.2014.09.020>
 17. Wang, J. F., Sun, Q. J., Wang, H., Liu, J. P., & Feng, J. C. (2016). Effect of location on microstructure and mechanical properties of additive layer manufactured Inconel 625 using gas tungsten arc welding. *Materials Science & Engineering A*, 676, 395–405. <https://doi.org/10.1016/j.msea.2016.09.015>
 18. Hack, H., Link, R., Knudsen, E., Baker, B., & Olig, S. (2017). Mechanical properties of additive manufactured nickel alloy 625. *Additive Manufacturing*, 14, 105–115. <https://doi.org/10.1016/j.addma.2017.02.004>
 19. Tanvir, A. N. M., Ahsan, M. R. U., Ji, C., Hawkins, W., Bates, B., & Kim, D. B. (2019). Heat treatment effects on Inconel 625 components fabricated by wire + arc additive manufacturing (WAAM)—part 1: Microstructural characterization. *The International Journal of Advanced Manufacturing Technology*, 103, 3785–3798. <https://doi.org/10.1007/s00170-019-03828-6>
 20. Tanvir, A. N. M., Ahsan, M. R., Seo, G., Kim, J. D., Ji, C., Bates, B., Lee, Y., & Kim, D. B. (2020). Heat treatment effects on Inconel 625 components fabricated by wire+ arc additively manufacturing (WAAM)—part 2: Mechanical properties. *The International Journal of Advanced Manufacturing Technology*, 110(7), 1709–1721. <https://doi.org/10.1007/s00170-020-05980-w>
 21. Yangfan, W., Xizhang, C., & Chuancho, S. (2019). Microstructure and mechanical properties of Inconel 625 fabricated by wire arc additive manufacturing. *Surface & Coatings Technology*, 374, 116–123. <https://doi.org/10.1016/j.surfcoat.2019.05.079>
 22. Wanga, Y., & Chena, X. (2019). Investigation on the microstructure and corrosion properties of Inconel 625 alloy fabricated by wire arc additive manufacturing. *Materials Research Express*, 6(10), 1–19. <https://doi.org/10.1088/2053-1591/ab39f6>
 23. Xu, X., Ding, J., Ganguly, S., & Williams, S. (2019). Investigation of process factors affecting mechanical properties of INCONEL 718 superalloy in wire + arc additive manufacture process. *Journal of Materials Processing Tech*, 265, 201–209. <https://doi.org/10.1016/j.jmatprotec.2018.10.023>
 24. Ravi, G., Murugan, N., & Arulmani, R. (2020). Microstructure and mechanical properties of Inconel-625 slab component fabricated by wire arc additive manufacturing. *Materials Science and Technology*, 36(16), 1785–1795. <https://doi.org/10.1080/02670836.2020.1836737>
 25. Kindermann, R. M., Roy, M. J., Morana, R., & Prangnell, P. B. (2020). Process response of Inconel 718 to wire+ arc additive manufacturing with cold metal transfer. *Materials & Design*, 195, 109031. <https://doi.org/10.1016/j.matdes.2020.109031>
 26. Kumar, A., & Maji, K. (2021). Microstructure and chemical composition analysis of double wire arc additive manufactured bimetallic structure. *Journal of Materials Engineering and Performance*, 30, 5413–5425. <https://doi.org/10.1007/s11665-021-05819-9>
 27. Wang, Y., Chen, X., Shen, Q., Su, C., Zhang, Y., Jayalakshmi, S., & Singh, R. A. (2021). Effect of magnetic Field on the microstructure and mechanical properties of Inconel 625 superalloy fabricated by wire arc additive manufacturing. *Journal of Manufacturing Processes*, 64, 10–19. <https://doi.org/10.1016/j.jmapro.2021.01.008>
 28. Chintala, A., Kumar, M. T., Sathishkumar, M., Arivazhagan, N., & Manikandan, M. (2021). Technology development for producing inconel 625 in aerospace application using wire arc additive manufacturing process. *Journal of Materials Engineering and Performance*, 30, 5333–5341. <https://doi.org/10.1007/s11665-021-05781-6>
 29. Kumar, A. (2022). Investigations on Similar, Dissimilar and Functionally Graded Materials Depositions using Double Wire Arc Additive Manufacturing. PhD Thesis, National Institute of Technology, Patna, India. <https://doi.org/10.5281/zenodo.7453838>
 30. Kumar, A., & Maji, K. (2019). Bead modelling and deposition path planning in wire arc additive manufacturing of three dimensional parts. *Materials Science Forum*, 969, 582–588. <https://doi.org/10.4028/www.scientific.net/MSF.969.582>
 31. Kumar, A., & Maji, K. (2020). Selection of process parameters for near-net shape deposition in wire arc additive manufacturing by genetic algorithm. *Journal of Materials Engineering and Performance*, 29(5), 3334–3352. <https://doi.org/10.1007/s11665-020-04847-1>
 32. Montgomery, D. C. (2001). *Design and analysis of experiments*. Wiley.
 33. Bosworth, M. R. (1991). Effective heat input in pulsed current gas metal arc welding with solid wire electrodes. *Welding J*, 70(5), 111–117.
 34. Ahsan, M. R., Seo, G. J., Fan, X., Liaw, P. K., Motaman, S., Haase, C., & Kim, D. B. (2021). Effects of process parameters on bead shape, microstructure, and mechanical properties in wire+ arc additive manufacturing of Al_{0.1}CoCrFeNi high-entropy alloy. *Journal of Manufacturing Processes*, 68, 1314–1327. <https://doi.org/10.1016/j.jmapro.2021.06.047>
 35. Ahsan, M. R. U., Kim, Y. R., Ashiri, R., Cho, Y. J., Eong, C. J., & Park, Y. D. (2016). Cold metal transfer (CMT) GMAW of Zinc-Coated steel. *Welding Journal*, 95, 120–132.
 36. Gupta, R. K., Kumar, V. A., Gururaja, U. V., Shivaram, B. R. N. V., Prasad, Y. M., Ramkumar, P., Chakravarthi, K. V. A., & Sarkar, P. (2015). Processing and characterization of Inconel 625 Nickel base Superalloy. *Materials Science Forum*, 830–831, 38–40. <https://doi.org/10.4028/www.scientific.net/MSF.830-831.38>

Publisher's Note Springer Nature remains neutral with regard to jurisdictional claims in published maps and institutional affiliations.

Springer Nature or its licensor (e.g. a society or other partner) holds exclusive rights to this article under a publishing agreement with the author(s) or other rightsholder(s); author self-archiving of the accepted manuscript version of this article is solely governed by the terms of such publishing agreement and applicable law.



Dr. Ashish Kumar is currently working as an Assistant Professor in Mechanical Engineering Department of JSPM Rajarshi Shahu College of Engineering, Tathawade, Pune, India. He obtained his M. Tech and Ph. D in Production Engineering from National Institute of Technology Patna in 2022. His areas of research are wire arc additive manufacturing, statistical modelling and optimization in additive manufacturing.



Mr. Ankit Shrivastava is a senior research fellow at CSIR-Central Mechanical Engineering Research Institute in India. He received his master degree in mechanical engineering. His research interests include sensorial monitoring of additive manufacturing for defect detection and control, laser material processing and friction stir welding.



Dr. Kuntal Maji is currently working as an Assistant Professor in Production and Industrial Engineering Department of National Institute of Technology Jamshedpur, India. He obtained his B.E. from Jadavpur University, India, M. Tech and Ph. D in Manufacturing Engineering from Indian Institute of Technology Kharagpur, India. His areas of research are wire arc additive manufacturing and incremental sheet metal forming.